

# Experimental measurements of a converging flux conserver suitable for compressing a field reversed configuration for magnetized target fusion

T. Intrator, M. Taccetti, D.A. Clark, J.H. Degnan<sup>1</sup>, D. Gale<sup>2</sup>, S. Coffey<sup>2</sup>, J. Garcia, P. Rodriguez, W. Sommars<sup>2</sup>, B. Marshall<sup>5</sup>, F. Wysocki, R. Siemon, R. Faehl, K. Forman, R. Bartlett, T. Cavazos<sup>2</sup>, R.J. Faehl, K. Forman, M.H. Frese<sup>4</sup>, D. Fulton, J.C. Gueits<sup>1</sup>, T.W. Hussey<sup>1</sup>, R. Kirkpatrick, G.F. Kiuttu<sup>1</sup>, F.M. Lehr<sup>1</sup>, J.D. Letterio<sup>1</sup>, I. Lindemuth, W. McCullough<sup>1</sup>, R. Moses, R.E. Peterkin<sup>1</sup>, R.E. Reinovsky, N.F. Roderick<sup>5</sup>, E.L. Ruden<sup>1</sup>, K.F. Schoenberg, D. Scudder, J. Shlachter, G.A. Wurden

Los Alamos National Laboratory, Los Alamos, New Mexico, United States of America

<sup>1</sup>Directed Energy Directorate, Air Force Research Laboratory, Kirtland AFB, New Mexico, United States of America

<sup>2</sup>Maxwell Technologies Inc., Albuquerque, New Mexico, United States of America

<sup>3</sup>NumerEx, Albuquerque, New Mexico, United States of America

<sup>4</sup>Department of Chemical and Nuclear Engineering, University of New Mexico, Albuquerque, New Mexico, United States of America

<sup>5</sup>Bechtel Nevada Inc., Las Vegas, Nevada, United States of America

E-mail: intrator@lanl.gov

Received 22 January 2001, accepted for publication 3 July 2001

Published 15 February 2002

Online at [stacks.iop.org/NF/42/211](http://stacks.iop.org/NF/42/211)

## Abstract

Data are presented that are part of a first step in establishing the scientific basis of magnetized target fusion (MTF) as a cost effective approach to fusion energy. A radially converging flux compressor shell with characteristics suitable for MTF is demonstrated to be feasible. The key scientific and engineering question for this experiment is whether the large radial force density required to uniformly pinch this cylindrical shell would do so without buckling or kinking its shape. The time evolution of the shell has been measured with several independent diagnostic methods. The uniformity, height to diameter ratio and radial convergence are all better than required to compress a high density field reversed configuration to fusion relevant temperature and density.

**PACS numbers:** 52.55.Lf, 52.58.-c

## 1. Introduction

Magnetized target fusion (MTF) could achieve fusion conditions by compressional heating of a magnetized target plasma inside an imploding flux conserver shell [1–5]. Pressures in the megabar range are accessible at the price of an intrinsically pulsed scenario. MTF requires a magnetized plasma target such as the field reversed configuration (FRC) as described by Tuszewski in a review article [6]. The liner

imparts energy via integrated  $\int P dV$  work that heats fuel by compressing it inside an imploding ‘pusher’ wall. A magnetic field embedded in the fuel thermally insulates it from the pusher.

The density regime and timescale of MTF is intermediate between those of magnetic fusion energy (MFE) and inertial confinement fusion (ICF). Lower density longer pulse tokamaks such as the planned ignition physics device ITER [7] operate at densities of  $n \sim 10^{14} \text{ cm}^{-3}$ . Another very

different possibility is ICF at very high density and pressure; for example, at NIF [8]. MTF has an intermediate density  $n_{MTF} \sim 10^{20} \text{ cm}^{-3}$ , with  $n_{MTF} \approx 10^6 n_{MFE} \approx 10^{-6} n_{ICF}$  at a temperature near 10 keV. Three technical considerations explain why the MTF regime is important. First, fusion reactivity scales as density squared, which can be increased by many orders of magnitude over conventional MFE. Second, all characteristic plasma scale lengths decrease with density. Hence, system size is naturally reduced at high density. Third, magnetic insulation greatly reduces the power and precision required to compressionally heat plasma to fusion relevant conditions compared with ICF, and brings the pulsed power requirements within reach of existing facilities [2, 9]. The technology and material properties rather than the physics of any of these concepts, including MTF, may well be factors that determine their eventual success. The engineering problems of pulsed power plant concepts required by ICF and MTF may turn out to be easier to solve than those of steady state concepts [2, 5, 10, 11].

The required cylindrical flux conserver is unusually long [12, 13] with an aspect ratio, or length to diameter ratio, of at least 3:1 to achieve fusion relevant parameters. We show here that it is possible to compress this shell uniformly to the required 10:1 radial convergence. The experimental data demonstrate the longest (>3:1 aspect ratio) successful experiment at the highest convergence (>13.5:1) that has ever been carried out to our knowledge. Experimental measurements with magnetic coil and Faraday rotation measurements of magnetic flux compression of a seed magnetic field show that the time histories of radial position and speed of an aluminium cylindrical shell are consistent with redundant diagnostics and a model. Fibre optic impact detectors show the symmetry and arrival time of the implosion. The radial symmetry appears to be better than 1%, i.e.  $\pm 300 \mu\text{m}$  out of an initial liner radius of 4.89 cm.

A large capacitor bank was used to drive an 11 MA axial current into the cylindrical flux conserver for the two experimental shots. The axial current density  $J_z$  generates an azimuthal magnetic field  $B_\theta$  outside the current surface and ohmically heats the shell as well. Computational models predicting a successful implosion exist [14] but have never been benchmarked for the long aspect ratio we need. The key scientific and engineering question for this experiment was whether the radial  $J_z \times B_\theta$  force density would uniformly pinch this large aspect ratio liner without buckling or kinking. The liner accelerates to an approximately terminal velocity driven by a peak magnetic field  $B_\theta$  of approximately 44 T, and a magnetic pressure of 7700 atm. An explosively imploded copper–tungsten flux conserver with large confined magnetic field has been shown to be dimensionally robust under extreme conditions [15]. A test including both a realistic magnetic field and a realistic plasma must wait for an integrated experiment compressing an FRC inside a liner. In this case the shell will ultimately stagnate against the interior plasma pressure. Instabilities of the Rayleigh–Taylor type would then be expected if the liner melted due to excessive ohmic dissipation as interior magnetic fields diffuse into the flux conserver.

The data given here comprise the first step in an attempt to establish the scientific basis of MTF as a faster and cheaper

## Magnetized Target Fusion

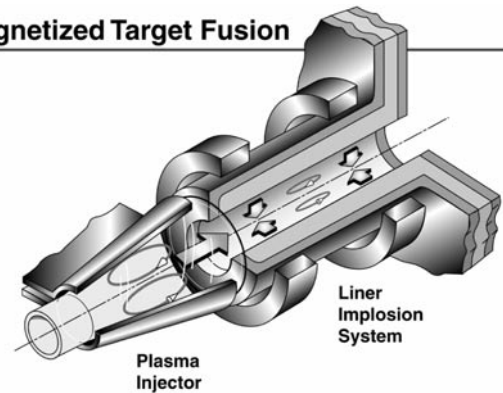


**Figure 1.** Schematic diagram of the MTF concept, showing plasma creation, its injection into the region with external flux conserver and its subsequent compression to fusion relevant temperatures and densities.

approach to fusion energy [10, 16–20]. To explore this concept, we are taking advantage of the past 20 years of compact toroid (CT) research in the MFE programme. The CT plasma chosen for the target is a high density FRC [16] similar to the early reversed field  $\theta$  pinch work on PHAROS [21, 22], JULIETTA [23, 24] and at Jülich [25]. As with earlier work at Los Alamos National Laboratory, we will translate the FRC into a compression region [26–28] but then compress it [11] using well established liner technology [9, 29–34] developed in US Department of Energy and Department of Defense research programmes in recent years. As sketched in Fig. 1 the closed magnetic surfaces of the FRC should provide enough thermal energy confinement during compression inside a metal liner flux conserver to allow compressional work and heating of the plasma to fusion relevant conditions. The lifetime of the FRC can be calculated with scaling laws [6] and the expected stability duration of 25–100 Alfvén transit times should provide adequate dwell time ( $>1 \mu\text{s}$ ) for the flux conserver to stagnate against the plasma pressure. Fusion energy will be generated in a microsecond pulse during which plasma pressure is magnetically and inertially confined by the imploding liner wall. The favourable stability scaling holds for the entire evolution from target FRC to the compressed high density and hot FRC. Small sized and high density fusion by MFE standards could achieve significant performance ( $n\tau_E > 10^{13} \text{ s cm}^{-3}$ ,  $T \approx 5 \text{ keV}$ ) in just a few years at modest cost using available pulsed power facilities.

In this article, Section 2 contains a description of the experimental hardware and diagnostics, as well as the assumptions we invoked to analyse the data. Section 3 discusses the data in terms of the shell trajectory and energy balance. The conclusions are summarized in Section 4.

## 2. Experimental description

### 2.1. Capacitor bank

The actual cylindrical flux conserving ‘liner’ implosion tests were carried out using the SHIVA star capacitor bank at the US Air Force Research Laboratory, Albuquerque, NM [35–37]. The two halves of the bank each have a capacitance of 2600  $\mu\text{F}$ , with the maximum voltage of nominally 60 kV

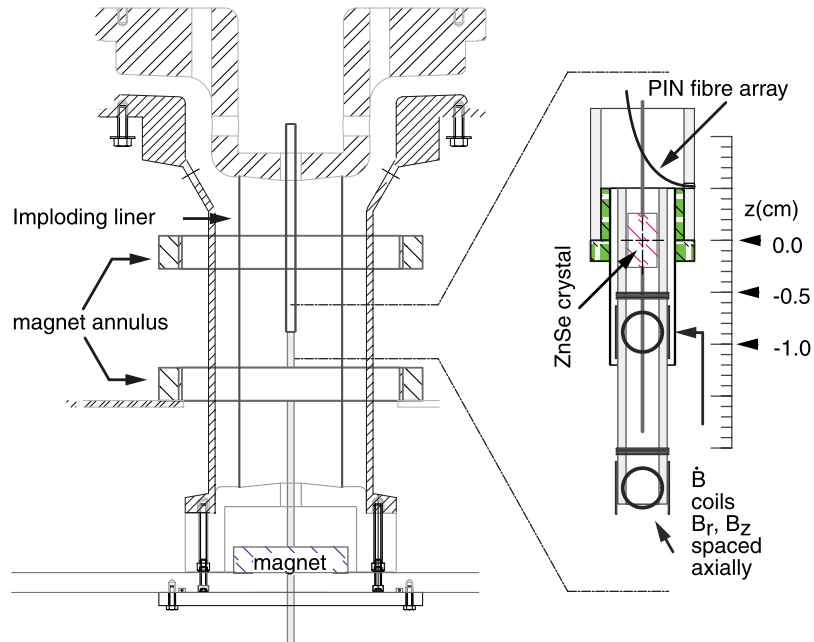


**Figure 2.** Schematic diagram of the cylindrical aluminium flux conserver, and the permanent magnet assembly consisting of a seed field pole piece on the bottom and two magnet annuli. The central column contained the magnetic field coil (bottom half), Faraday rotation (midplane) and the fibre optic impact detector (top half) probes. The magnified view of the midplane region shows the exact placement and orientation of some of these probes.

that we operated with, one half swinging positive and one half swinging negative. The applied final voltage had a doubled Marx bank value of 80 kV. With a conservative 40 kV charge per bank we had 4.2 MJ available for this experiment. We estimate that 1.4 MJ of kinetic energy was delivered to the imploding shell. This was 33% of the initial capacitor bank stored energy.

The SHIVA circuit includes low inductance star configuration current feeds that converge to the load. The bank can tolerate 75% voltage reversal, and has a bank plus transmission line inductance of 3 nH, making a total system inductance including the load of 44 nH, with a resistance of approximately 1 m $\Omega$ . This ringing LC tank circuit is normally used with a series safety fuse that heats up so that the increased resistance limits the current in fault mode to 40 MA. Direct discharge currents in past experiments have ranged from 12 to 15 MA into implosion loads to 30 MA for driving inductive store opening switch loads. Current rise times range from 3 to 10  $\mu$ s, depending on load inductance.

## 2.2. Liner design and drive

The liner chosen for this experiment had a higher length to diameter ratio (aspect ratio) than that for any previous liner experiment. A large aspect ratio will allow enough space for the full length of an FRC to propagate into the flux conserver region before the liner implodes fully. We chose the liner thickness so that resistive heating (at least for this experiment) would not cause excessive bulk heating. Analytic criteria such as those used by Maisonnier et al. [38] to avoid the onset of vaporization (or melting in our case) were checked using the MHD code Mach2 [39] for 1-D and 2-D MHD simulations. As long as the liner remains solid, material strength can

stabilize the liner against instability growth (at least in the 2-D approximation), provided initial imperfections in the initial geometry of the liner are sufficiently small [40]. We obtain good agreement between the above sophisticated calculations and simpler circuit calculations assuming finite incompressible shell thickness with interactive inductance and safety fuse resistance [37, 40]. The timing of the contact between the liner and central probe package can be predicted to a precision of less than several hundred nanoseconds.

The shell length was 30 cm and the outside diameter was 10 cm to match our FRC design. It was fabricated from a solid rod of aluminium alloy with good machining properties (6061-T6), and machined outside and inside using a mandrel for good concentricity and uniform wall thickness. Extrusion would be a cost effective option if many of these shells were to be fabricated. The lathe finish was 0.762  $\mu$ m and slightly buffed to a polish. The dimensions were a nominal 9.78 cm inside diameter and 1.1 mm wall thickness, with square and smooth ends. The mass was 0.27 kg.

The ends of the shell were designed to fit tightly against a glide plane that had a 6 $^\circ$  conical taper to provide a good (but sliding) electrical contact for the axial current driven by the SHIVA capacitor bank. The electric current originates in a star shaped array of capacitor banks that converge to the centre, which houses a cylindrically symmetric vacuum transmission line. The transmission line converges to the axis where the centre conductor connects to the top glide plane and the return coaxial feed surrounds the centre and connects to the bottom glide plane. The nominal room temperature conductivity of this alloy is 3.8  $\mu\Omega$  cm, and the calculated inductance for the axial current was approximately 300 nH. The liner was fitted tightly in between the glide plane conical tapers with an axial compression of 3 mm out of the 30 cm length, engendering good electrical contact with the glide plane. This

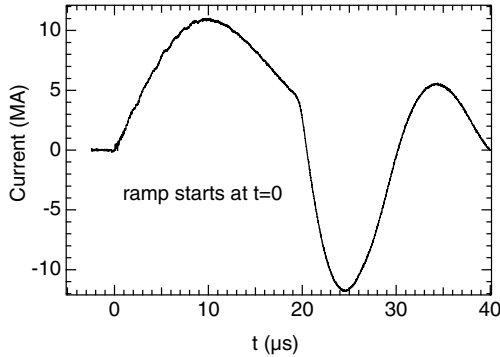


**Figure 3.** Time development of the current delivered to the liner by the SHIVA bank, with  $t = 0$  defined as the initiation of current ramp.

gave rise to a force of 1600 N calculated to compress the liner (without buckling) to less than 4% of the buckling threshold. A schematic diagram of the cylinder shell, glide plane and centre axis diagnostic assembly with a midplane expanded detail is shown in Fig. 2.

The final axial drive current into the liner had a maximum of 11 MA for the two experimental shots approximately 10  $\mu\text{s}$  after the current ramp was initiated. An azimuthal magnetic field outside the current surface ohmically heats the shell as well. It turned out that the radial  $J_z \times B_\theta$  force density did uniformly pinch this large aspect ratio liner without the occurrence of buckling or kinking. The liner accelerates to an approximately terminal velocity of 0.45 cm/ $\mu\text{s}$ . The axial current shown in Fig. 3 peaks halfway through the shot. The radial accelerating force subsequently decreases swiftly as the square of the drive current. This corresponds to a peak axial current generated magnetic field  $B_\theta$  of approximately 44 T and a magnetic pressure of  $B_\theta^2/2\mu_0 \approx 770 \text{ MPa}$  ( $\approx 7700 \text{ atm}$ ).

### 2.3. Vacuum chamber, conditions and liner generated plasma

This experiment was carried out in nominal high vacuum conditions, with a base pressure near  $10^{-6}$  torr. The valves for the vacuum system were closed several minutes prior to the capacitor trigger, and a slow leak into the experimental chamber was allowed. The actual neutral pressure at the time of the shot was near  $4 \times 10^{-6}$  torr. The transmission line is insulated on the air side with Formvar and the rest of it is vacuum gapped and magnetically insulated. The primary concern is that one does not want the transmission line or any other point between this line and the liner load to arc. The product of pressure  $P$  times spark gap  $D$  needs to be low enough that the Paschen curve criterion for discharge breakdown is not near the minimum voltage, i.e. not near  $PD \approx 1 \text{ torr cm}$ .

No intentional plasma was present during the shot, although the liner sliding on the glide plane during implosion generates copious arcs, sparks, photons from the visible all the way up to soft X ray energies, and probably a high density aluminium plasma as well. The light from this discharge is extremely bright. Optical, VUV or SXR diagnostics viewing at this region need to have some type of light-tight cap on them to avoid being blinded prematurely by the flash. The effects of these impurities on the actual FRC compression have never been considered in detail. One could imagine a deformable

cylindrical flux compressor design that does not require sliding contacts, thus avoiding this whole issue.

The vacuum chamber is described elsewhere [37] and is constructed of aluminium 6061 alloy, with 1 in. walls and rectangular ports for diagnostics such as X ray sources and film. It is bolted onto the bottom of the transmission line assembly in the centre of the star electrical feeds. The top and bottom of the chamber is lathe cut after each shot to smooth out the blasted contours and provide a uniform sealing surface for the O ring vacuum seals.

### 2.4. Diagnostics

**2.4.1. Diagnostic package on-axis** Several redundant diagnostics allowed us to infer the flux conserver shell radius, shape, concentricity and uniformity as it radially converged to the axis. MTF with an FRC as a magnetized plasma target requires an exceptionally long liner with length to diameter ratio of at least the 3:1 example we demonstrate here. Buckling, non-uniformity of radial contraction, tearing and instabilities were all postulated as possible failure modes of this experiment. The typical aspect ratio for liner experiments is usually closer to 1:1. The data we show here document the longest ( $>3:1$  aspect ratio) liner experiment that has ever been carried out.

Down the centre axis of the shell, we installed two diagnostic stalks, one from the top and one from the bottom. They both joined near the liner midplane. As shown in Fig. 2 the top 1 cm diameter stalk included an array of four fibre optic impact detectors (FIDs) arranged azimuthally near the top (glide plane), another array of four at the midplane, and an axial array between the glide plane and the midplane. The axial array contained 12 FIDs spaced linearly between the glide plane and the midplane. These measured the liner time of impact via the optical emission due to shock heating in the fibres [41]. The stalk diameter near the FIDs could not be any smaller than 1.0 cm because the optical fibres were already at their minimum bend radius when installed in the stalk. The top half of the liner stopped here at a 9.78/1 radial compression ratio. The bottom 0.635 cm diameter stalk included arrays of magnetic loop ( $\dot{B} \equiv dB/dt$ ) probes and allowed the liner to travel to a full 9.78 cm/0.635 cm = 15.4:1 radial compression ratio before stopping on the central stalk. Through the center of both stalks we routed an optical fibre for use with a novel ZnSe Faraday rotation sensor. The two stalks were joined at a concentric bushing. We provided a small background magnetic seed field that was compressed as the liner contracted radially.

Measurements of the magnetic field with magnetic field coil and Faraday techniques provided a redundant way to determine the time evolution of the liner radius. FIDs determined the arrival time at a predetermined radius, and radiographs showed snapshots of the liner shape at several selected times. All the data agree quite well.

**2.4.2. Background magnetic seed field and its compression by the liner** Magnets similar to refrigerator magnets were used for the permanent axial magnetic field that varied from 0.006 to 0.009 T throughout the interior of the liner region of interest and was eventually compressed to 0.4 T or more. In a real FRC compression experiment, the trapped compressed magnetic

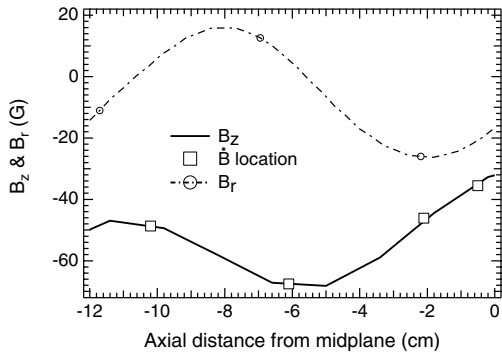


**Figure 4.** Magnetic seed field profiles at a radius near the (initial ( $t = 0$ )) inner surface of the flux conserver shell.

field would be of the order of 200–500 T. This magnetic field pressure would be sufficient to cause the inward motion of the shell to stagnate. We chose a small seed field that was easy to implement with the sole purpose of facilitating the inference of flux conserver radius from magnetic measurements. The axial and radial components of the magnetic field were measured with a Hall probe and modelled with a magnetostatic code [42].

As this field was compressed by the contracting shell, we measured both components of  $\mathbf{B}$  near the axis inside the detector stalk. The magnetic field distribution  $B_r(z)$  and  $B_z(z)$  at  $t = 0$  at the liner radius is shown in Fig. 4, with more details given by Taccetti et al. [42]. This impressed seed field can be altered by the azimuthal image currents in the liner. Therefore our initial presumption that  $B_z(z)$  was locally constant would require this type of correction to carry out a more subtle calculation of liner radius from  $\mathbf{B}(t)$  evolution.

As seen in Fig. 5 both components of the dominant axial  $B_z$  and smaller  $B_r$  field grew as the flux compressed. This observation motivated us to consider the magnetic fields induced by the image currents induced in the reference frame of the moving liner. Since the  $\mathbf{B}$  field is divergence free, there must be temporal changes (i.e. time derivatives) in the radial components as well as for the axial components of  $\mathbf{B}$ . If we use Faraday's law to consider the electric fields induced by time varying radial magnetic fields in cylindrical geometry then

$$(\nabla \times \mathbf{E})_r = (1/r)\partial E_z/\partial\theta - \partial E_\theta/\partial z = -\partial B_r/\partial t. \quad (1)$$

In the moving frame of the flux conserver the time derivative including the convective part is  $\partial/\partial t = \partial/\partial t + \mathbf{v}_r \cdot \partial/\partial r$ . Any radial ray that pierces a region in the shell where this convective term is large will thus have eddy currents that circulate about it. Looking inwards at this ray, such a circulation loop would have components that are sequentially azimuthal (e.g. clockwise  $E_\theta$  and  $J_\theta$  at the bottom), axial (e.g.  $E_z$  and  $J_z$  in the positive  $z$  direction on the left side), opposite azimuthal (e.g. anticlockwise at the top) and finally axial to close the loop (e.g. negative  $z$  direction on the last side). The  $J_z$  from neighbouring eddy currents will cancel leaving only counter-circulating currents at the top and bottom of the cylinder. This will impart some axial gradient to the final  $B_z$  field. For the eventual FRC compression experiments, any  $B_r$  frozen into the flux conserver could have a large effect. More information about this question will be found in Taccetti et al. [42].

We estimate the azimuthal electric field  $E_\theta$  by integrating Eq. (1) over some fraction of the cylinder surface  $E_\theta(2\pi r) \approx$

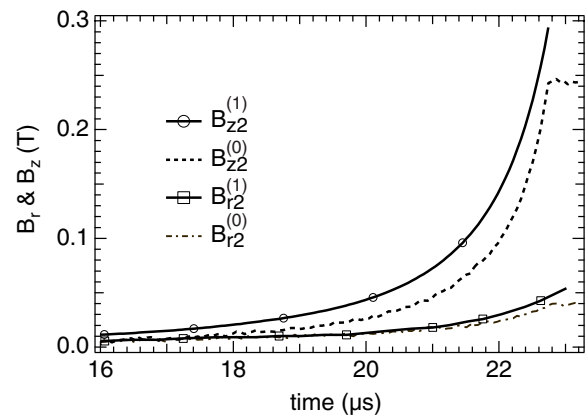


**Figure 5.** Typical magnetic field measurements extracted from magnetic field coil data showing time delay and amplitude corrections from the skin depth and flux dissipation calculations. The liner radius struck the cylinder shield at approximately  $t = 23.4 \mu\text{s}$ .

$-(dB_r/dt)2\pi rh$ , where  $B_r$  does not change much. Here  $h \approx B_r/(\partial B_r/\partial z) \approx 10$  cm is the axial scale length for changes in  $B_r$  from Fig. 4 and  $dB_r/dt$  is computed from the curve fit  $B_r(t)$  in Fig. 5. This corresponds to approximately 10 loop volts around the compressed liner, which is less than the 40–60 loop volts estimated from the compression of axial flux, and very much less than the 80 kV bank voltage driving the axial liner current.

**2.4.3. Fibre optic impact detectors** The time of impact of the liner near the axis was measured optically. The fibre optic impact detector (FID) was a glass  $100 \mu\text{m}$  fibre [41] whose end was polished and covered by an opaque  $25 \mu\text{m}$  aluminium foil. We used azimuthal arrays at both the glide plane and the midplane, with one axial array between these two azimuthal arrays. The fibre end is mounted inside a  $0.75$  mm diameter  $\times$   $2$  mm long stainless steel capillary tube and then mounted with its face pointing radially outwards on the central measurement stalk as shown schematically in Fig. 2. When the liner arrives at the FID fibre, the shock heats the end and the fibre emits a burst of optical black body radiation. The fibre leads to a photomultiplier preamplifier with quasi-logarithmic response. A fast rising signal with no precursor signifies a solid metal impact. This furnishes a precise measurement of the impact time, with a resolution in this application of 20–50 ns (although much better resolution is possible). The sharp rise time of the shock signal is usually unambiguous unless there is a temporally smeared shock front, as was the case for our FIDs installed near the glide plane.

The optical signal was routed into the screen room control centre via 60 m of fibre, and then converted to electrical signals. These were amplitude calibrated to each other, and time synchronized for trigger and group delay. The electrical signals in the screen room were digitized on VXI Tektronix TEK641 recorders at 4 ns per sample, with data records of 15 000 samples, eight bits deep. As shown in Fig. 6 the midplane and glide plane azimuthal arrays each had four optical fibres  $90^\circ$  apart and the ten fibre axial array shared two of these fibres. All times in our data refer to the start of the current ramp in

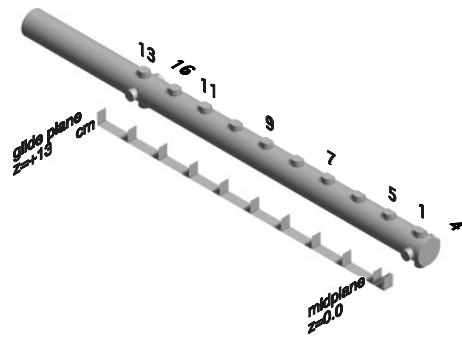


**Figure 6.** Schematic diagram of the two FID azimuthal arrays, one at the midplane (1–4, 1 and 4 called out on figure), one at the glide plane (13–16, 13 and 16 called out on the figure) and the axial array (1, 5–16, 13). Some of the identification numbers are omitted as they would obstruct the view.

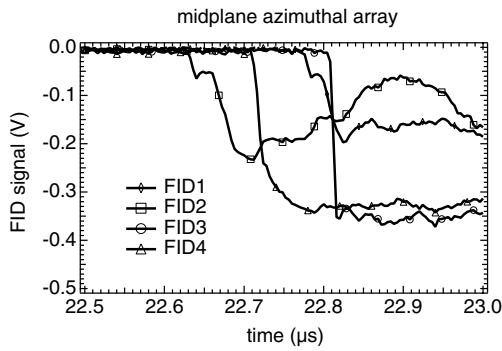


**Figure 7.** FID data near the midplane showing the abrupt rise in signal at the time of impact.

Fig. 3 as time  $t = 0$ . Impact arrival times are estimated at 20% of the first maximum excursion in the FID signal.

All the FIDs were installed in two azimuthal arrays and one axial array in the top half of the diagnostic package cylinder, which was 1.0 cm in diameter, and projected 14.5 cm into the liner region from the top. The bottom of the cylinder had a ‘top hat’ end bushing that fitted inside the end of the cylinder, forming an end square to the cylinder axis. This bushing was bored to accept the 0.635 cm diameter stainless steel (SS) tube that contained the magnetic field coil diagnostic package that extended from the bottom glide plane up to the midplane.

Figure 7 shows the arrival times of the midplane azimuthal array, from which we infer the circular uniformity. The glide plane arrival times are considerably more ambiguous as shown in Fig. 8. This is probably because the continuous arcs, sparks and local aluminium plasma compete with the impulsive shock heated fibre signal. The converging shell at the midplane remained within 0.6% of being perfectly circular, as shown by Fig. 9. Here we have spline fitted the azimuthal FID data for channels 1–4 and compared them with a reference circle. There also may be some mixture of  $m \geq 2$  deformations. The time delays from Fig. 7 were converted to distance for Fig. 9 (Section 3.1) by estimating a final radial velocity of 0.4 cm/ $\mu$ s inwards at the time of impact. The radial runout was less than  $\pm 0.3$  mm out of an initial circular radius of 48.9 mm, or more pessimistically 6% of the 5 mm radius at the time of impact. The circular uniformity of the glide plane end of the aluminium

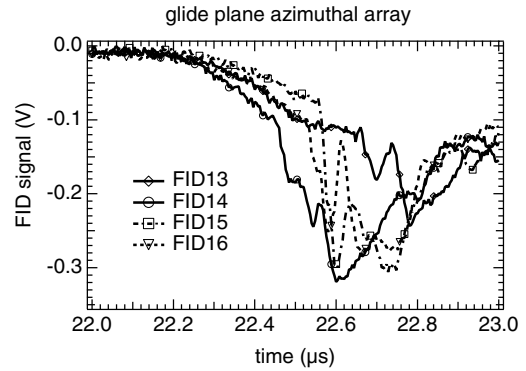


**Figure 8.** FID data near the glide plane showing the gradual rise in signal and the ambiguous time of impact.

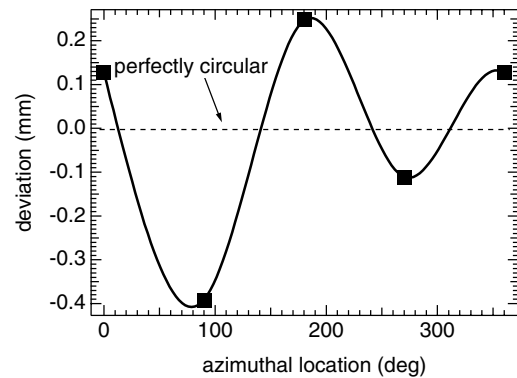


**Figure 9.** Deviation of spline fit (curve) to a reference circle for FID data (squares) near the midplane. Distortion modes of  $m = 2$  or larger may exist.

shell was hard to estimate because the shock arrival times were less well defined.

Data from the axial array are shown in Fig. 10(a) where the liner at the glide plane end is seen to arrive earlier (on the average) than at the midplane end. Some of this difference is due to the local plasma light signal at the glide plane, but there may be some conical shaping of the liner. These data are summarized in Fig. 10(b), where the axial uniformity of the top half of the converging shell can be estimated using the computed radial velocity that we will show later in Fig. 16.

**2.4.4. Magnetic probes** We describe here how we inferred the flux conserver radius from the measured changes in an initially static seed magnetic field. An axial magnetic probe array was shielded electrostatically inside a 0.635 cm diameter SS tube with 0.25 mm walls. As the initially static magnetic field was compressed inside the flux conserver (but outside the SS shield), it soaked into the SS shield. The magnetic probes inside the shield thus detected a time delayed and attenuated signal, from which we computed the time dependent field outside the shield.

At each of five axial locations spaced from the bottom glide plane up to the midplane, there were axial  $B_z$  and radial  $B_r$  magnetic coils. These axial locations were  $z = -0.5, -2.1, -6.1, -10.6$  and  $-14.5$  cm from the midplane. Coils were overlaid in wound/counterwound pairs to give us differential signals so we could take advantage of common mode rejection

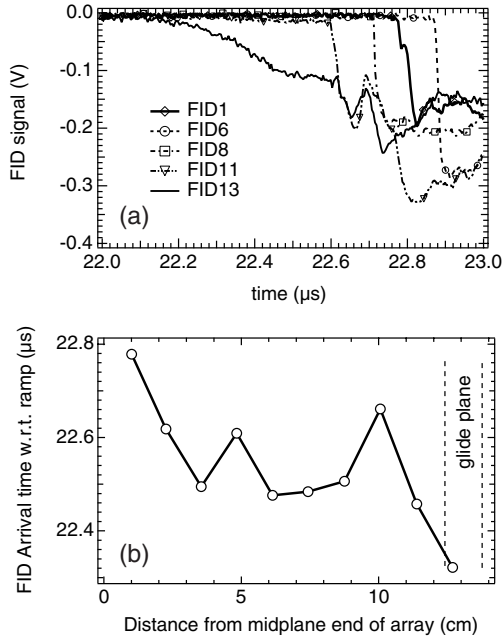


**Figure 10.** (a) FID data for axial array showing gradual transition from sharp to smeared arrival times of the impact shock signal. (b) Synopsis of FID data for the entire axial array showing the arrival times along the axial length of the diagnostic package.

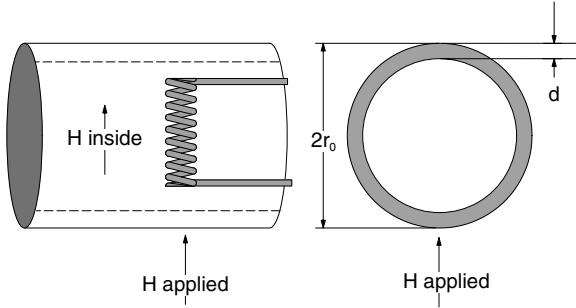


**Figure 11.** Schematic diagram of the magnetic coil probe inside the cylindrical conducting shell, showing an example of the ‘applied’ magnetic field outside the conducting shield and the attenuated and time delayed field inside the shield. The geometry for the correction calculation invokes the shell radius  $r_0$  and thickness  $d$ . The calculation in Eq. (3) is valid for  $H(\text{applied})$  being either radial or axial ( $\beta = 0$ ).

(CMR) by taking sums and differences of the signals. Owing to our high bandwidth (GHz) low-bleed-through integrators [42], CMR turned out to be less of a problem than we had initially thought.

The radius of the liner was inferred from the increase in  $B$  field measured with the magnetic field coil array. It turned out that the magnetic field coil probes at  $z = -14.5$  cm were buried in the glide plane so that these data were not used in subsequent analyses. Flux conservation was initially assumed and our calculations for the correction of this presumption are outlined below.

Even though the initial seed field created by the permanent magnet array shown in Fig. 2 was static, the moving boundary creates a time dependent behaviour. The SS tube around the magnetic coil probe adds attenuation and time delay as magnetic field diffuses through the cylindrical wall with the

geometry shown in Fig. 11. We had to deconvolve the response of the shielded probe by solving the Fourier transformed time dependent diffusion problem in cylindrical geometry. We then inverse transformed the data back into the time domain. If one assumes that the applied ‘external’ magnetic field (i.e. external to the SS shield tube and internal to the flux conserver shell) has Fourier components at frequencies  $\omega$

$$H(\omega) = H e^{-i\omega t} \quad (2)$$

then the ratio of the outside field (that compressed outside the probe shield) to the inside field (that attenuated and time delayed inside the probes shield) can be expressed as the solution of a diffusion equation [43, 44],

$$H_{out}/H_{int} = \cosh(kd) + (1/2r_0k)[1 + \beta/(kr_0)^2 \sinh(kd)] \quad (3)$$

where  $\beta = 0$  if  $B = B_z$  and  $\beta = 1$  if  $B = B_r$ . The wall thickness was  $d = 0.25$  mm ( $\ll r_0$ ), with a resistivity for the SS tube of  $70 \mu\Omega$  cm. The inverse skin depth  $k$  is conveniently written as

$$k(\omega) = 1/\delta = (1+i)(\mu_0\omega\sigma)^{1/2} \quad (4)$$

where  $i^2 = -1$ ,  $\sigma$  is the conductivity,  $\mu$  the magnetic permeability and  $\omega$  the angular frequency. These results can then be inverse Fourier transformed from  $H(\omega)$  back to the time domain  $H(t)$ . An example of this correction was shown in Fig. 5, which compares typical raw data (dashed and chain curves) measured inside the shielding tube with the time and amplitude corrected values (solid curves) outside the shield. The attenuation and time delay is apparent here for both axial  $B_z$  and radial  $B_r$ .

Note that radial compression of the boundary increases the  $B$  field for both axial and radial components. We used the  $B$  data from the integrated signal from the magnetic coils,

$$B(t) = B(t=0) + \int [dB(t')/dt'] dt' \quad (5)$$

where  $B(t=0, r)$  was measured and mapped out prior to the experiment, and the integration was carried out with a passive GHz bandwidth low inductance device fabricated in-house [42]. Our lowest order estimate of the liner assumed that axial flux was conserved so that

$$r(t) \approx r(t=0)[B(t=0)/B(t)]^{1/2}. \quad (6)$$

Corrections invoking the radial fields were calculated and turned out to be small. We also checked to make sure that this correction did not make the divergence of  $B$  much different from zero. More discussion of the magnetic coil data will follow as we summarize the agreement of all the diagnostic results.

**2.4.5. Faraday sensor** In an electrically noisy experiment such as this, optical diagnostics have the advantage of immunity to electromagnetic interference. We describe here a novel Faraday sensor used to measure the magnetic field on-axis. For some magneto-optic materials [45] the phase lag  $\Delta\phi$  between left and right hand circularly polarized components can be significant and is proportional to the integrated  $\Delta\phi$  (=

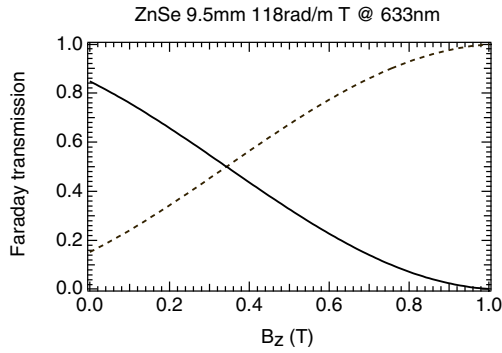


**Figure 12.** Faraday calibration and the location of the operating point at  $B_z = 0$  T.

$\int B_z dz/\lambda$  along the direction of the magnetic field  $B_z$ . We chose a 9.5 mm long ZnSe crystal with a high Verdet constant of  $V = 118$  rad/(m T) at the pump laser wavelength  $\lambda = 633$  nm. A HeNe laser provided randomly polarized light which passed through an optical fibre to the miniature Faraday detector embedded in the central diagnostic package shown in Fig. 2. A polarizer splitter on the input side of the Verdet crystal separates the laser light into two orthogonal linear polarization components, which are linear combinations of the circularly polarized components. The Verdet crystal shifts the polarization angle of each linear polarized component as a function of the magnetic field at the crystal (increasing with time). Polarizers on the output of each end yield intensity modulated signals that are brought out on two fibres which exit the vacuum can via epoxy seals to the screen room, where the pump laser was also situated. Light focusing in this small package was accomplished using tiny graded refractive index (GRIN) lenses as sections of the optical fibres.

The operating point of the polarizers was set close to the linear portion of the cosine curve (output polarizer  $\phi_{pol} = 23^\circ$  rotation with respect to the input polarizer). The calibration curve is shown in Fig. 12, where the solid and dashed curves correspond to the transmission fractions for each leg of the input splitter. The intensity transmission factors are  $T_2 = [\cos(2VB + 2\phi_{pol}) + 1]/2$  and  $T_1 = 1 - T_2$ . Here  $V$  is the Verdet constant,  $B$  the axial magnetic field immersing the ZnSe crystal and  $\phi_{pol}$  the polarizer angle. The range of this diagnostic stretched from approximately 0.04 to 1 T with high sensitivity, immunity from electrical noise and low noise floor. This approach could measure much larger fields with a more stable laser, shorter crystal and DC drift compensation.

The Faraday crystal was located at  $z \approx -0.5$  to  $+0.5$  cm from the midplane, and was immersed in a background magnetic field from the permanent magnet structure. This  $B_0$  field was slightly larger ( $\approx 10\%$ ) than the field at the magnetic coil probe ( $B_1$ ) nearest the midplane. These two diagnostics ought to measure close to the same values for the magnetic field. A comparison of these data in Fig. 13 shows the raw data and the same signals corrected for the diffusion time and attenuation. Good agreement is evident.

**2.4.6. Radiographs** Flash radiography provided snapshots of the progress of the converging shell through the 0.64 cm thick, 10 cm inner radius aluminium outer return current

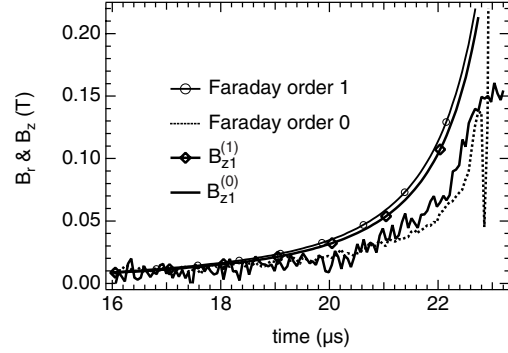


**Figure 13.** Faraday  $B_z$  data at the midplane compared with the adjacent magnetic coil probe data. The raw and corrected (time and amplitude) data are in good agreement with each other.

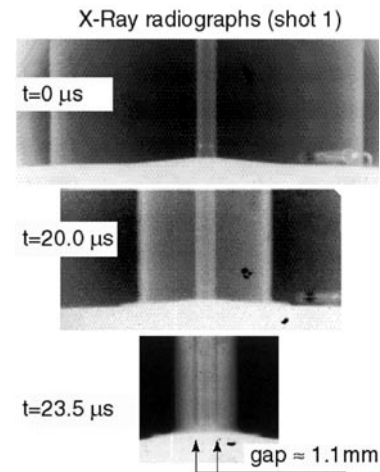


**Figure 14.** Side-on radiographs near the lower glide plane of the initial liner and at three times,  $t = 0.0, 20.0$  and  $23.5 \mu\text{s}$ , during implosion. The 0.64 cm stationary probe jacket containing magnetic and optical probes is visible on-axis.

conductor. Radiographs were taken at two different times, 20.0 and 23.5  $\mu\text{s}$ , after the start of the current ramp for the first shot. At each of these times, two axial positions were imaged, both at the midplane and at the glide plane. A set-up shot showing the initial conditions provides a  $t = 0$  reference. The X ray shadow of the 0.635 cm diameter probe package provides a useful size scale for the radiographs. The X ray source was a 300 kV, 5 kA, 30 ns pulse that was drawn to a tungsten anode [35–37]. Radiograph negative exposures in Fig. 14 show excellent symmetry of the implosion within the  $\approx 0.02$  cm resolution of the diagnostic.

### 3. Data analysis

#### 3.1. Trajectory and symmetry of the flux conserver

The shrinking radius of the flux conserving boundary can be inferred from the measured time evolution and growth of the trapped magnetic seed field created by the permanent magnet structure. Typical time integrated (using hardware integrators)  $B(t)$  data from the axial magnetic coil array were shown in Fig. 5, where  $B_{z1}$  is at  $z = -0.5$  cm and  $B_{z2}$  is at  $z = -2.1$  cm from the midplane. The radius at each axial location is calculated in steps, starting with a zero order quantity  $r(0)(t)$

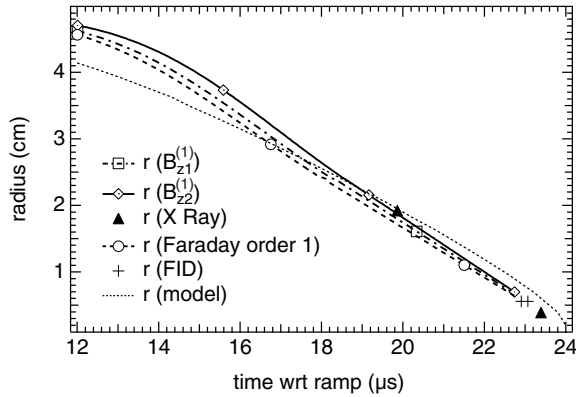


**Figure 15.** Time development of the inferred shell radius near the midplane. Data from magnetic field coil, Faraday, FID and radiographs are overlaid, and are quite consistent with each other.

that invokes the presumption that the axial flux is conserved. We rewrite Eq. (6) to lowest order

$$r^{(0)}(t) = r^{(0)}(t=0)[B_z^{(0)}(t=0)/B_z^{(0)}(t)]^{1/2}. \quad (7)$$

The time evolution of the  $B_z$  data such as those shown in Fig. 5 (corrected for skin depth diffusion delay and attenuation) is used for Eq. (7). The flux dissipation due to induced image currents in the liner from the increasing magnetic field is also accounted for, with details in Section 3.2. The ‘missing’ flux is added back to the measured quantity before we calculate the first order corrected radii  $r^{(1)}(t)$  plotted in Fig. 15 at  $z = -0.5$  and  $-2.1$  cm from the midplane. Overlaid on this plot are radius data derived from the X ray radiographs, the FID arrival times at  $r = 0.5$  cm and the Faraday rotation data. A prediction of the liner radius trajectory from an incompressible liner model with a reasonably complete capacitor bank, fuse and transmission line circuit (i.e. no free parameters) is also shown for Ref. [36].

Agreement is quite good, and discrepancies are probably due to details of the SHIVA bank current waveform differing slightly from the model assumptions. The spread in experimental data results gives an estimate of reasonable error bars to put on this plot. For times before  $t \approx 14 \mu\text{s}$ , the noise in the signal is significant enough that the zero baseline is uncertain for the data. Since the data analysis requires one to divide by the baseline offset (i.e. close to zero at early times), the errors in derived radii are large at earlier times.

The  $B_z$  data are fitted to a curve using two singular non-linear least squares fit iterations. A time is fitted for each data set near  $24 \mu\text{s}$  to yield a pole of order two for the curve fit routine. This is consistent with the prediction of Eq. (7) if the radius must tend to zero at the singularity time. A low order polynomial fit is also added to model the early time behaviour, and there is consequently a kink in the derivatives near  $t \approx 18 \mu\text{s}$ . This allows us to compute low noise time derivatives to obtain the liner radial velocity without smoothing out the interesting features. The terminal speed from Fig. 16 appears to be approximately  $0.38\text{--}0.43 \text{ cm}/\mu\text{s}$ , in spite of the uncertainty in the derivatives of the data. The radial velocity inferred from the X ray images in Fig. 14 is approximately  $0.44 \text{ cm}/\mu\text{s}$ . The model actually predicts constant acceleration inwards, as long as non-zero  $J \times B$  forces are driving the

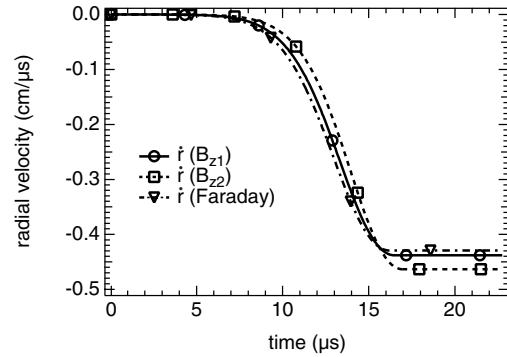


**Figure 16.** Time development of the inferred shell velocity. Data from  $\dot{B}_1$  ( $z = -0.5$  cm) and  $\dot{B}_2$  ( $z = -2.1$  cm) are overlaid and are quite consistent with each other.

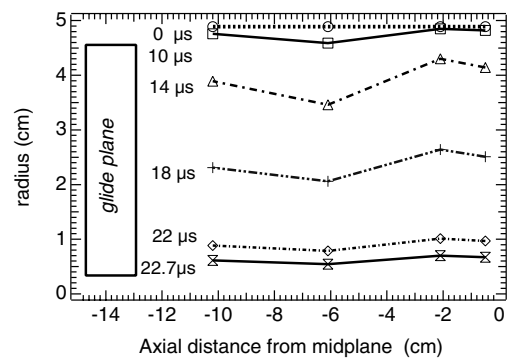


**Figure 17.** Axial profiles of the liner shape inferred from magnetic field coil probes for a series of times during the compression pulse. The symbols corresponding to  $t = 0, 10, 14, 18, 22$  and  $22.7 \mu\text{s}$  are, respectively, circles, squares, triangles, crosses, diamonds and bow ties. The errors for early times are large because the signals are small.

shell. This velocity would be asymptotic to the terminal velocity as the current waveform crosses zero, but we cannot experimentally resolve any curvature in Fig. 15 after  $t \approx 16 \mu\text{s}$ .

The axial shape of the flux conserver was fairly uniform as it radially contracted during the shot. In Fig. 17 we show the liner radius inferred from magnetic coil data extracted at even time intervals of  $4 \mu\text{s}$ , for  $t = 10, 14, 18, 22 \mu\text{s}$ . We also include a  $22.7 \mu\text{s}$  profile just before the shell fully imploded. The errors in calculated radii for times earlier than  $18 \mu\text{s}$  are significant because of the baseline zero uncertainty. For the later time slices the zero to peak variation in the liner radius was approximately  $0.5 \text{ mm}$ . This is a slightly larger deviation from roundness than the radial uniformity estimate from the FID data. On the other hand, the errors from the magnetic coil data and analysis are probably larger than any timing errors associated with the FID data sets. We do not include data from the magnetic coil probe at  $z = -14.2$  cm from the midplane, because the magnetic field it measured was significantly affected by the nearby ss glide plane conducting boundary.

Good cylindrical symmetry of the shell is evident from the radiographs shown in Fig. 14. Because the aluminium is approximately incompressible, conservation of mass implies the increase of liner thickness observed here. The grey scale density varies from light (minimum chord averaged X ray transmission) to dark (maximum chordal transmission). The

inside radius of the aluminium shell ( $r = 4.32$  mm) was taken to be that radius outside the dark vertical stripe indicated by the arrows at which the measured grey scale reached the lightest shade. Note the 0.11 cm gap between the inner surface of the liner and the stationary probe jacket at  $23.5 \mu\text{s}$ . This indicates acceptable symmetry with a measured radial compression ratio of 11.3:1, and an inferred 15:1 compression to the 3.17 mm magnetic coil package radius. These data exceed the 10:1 design goal for MTF compression of an FRC.

### 3.2. Flux dissipation inside the resistive liner

The original data analysis showed that the magnetic probe data experienced some cataclysmic demise over half a microsecond before the shell converged and smashed into the stalk holding the magnetic probe arrays. There were several possibilities. If large amounts of magnetic flux were dissipated, the correction could decrease the apparent liner radius inferred from the magnetic field measurements. The timing could also be in error. The analysis in this section eliminated the first possibility, and no problems could be found with the timing. Rather we concluded that the probe array was destroyed before the shell crashed into the probe stalk, possibly by some precursor metal ‘foot’ preceding the liner trajectory on the bottom glide plane. In this section we develop a simple quasi-analytic model directly related to our data so that we can estimate the image currents induced in the moving flux conserver. Energy balance considerations are also discussed.

The trapped magnetic field inside the conducting shell must induce azimuthal image currents (and for non-uniform fields, axial image currents) on the inside surface of the liner. Ohmic heating then raises the shell temperature and resistivity. For the eventual FRC compression inside the imploding flux compressor, this ohmic heating will melt the shell at the end of the stagnation dwell time. Then flux will diffuse through the liner and Rayleigh–Taylor type instabilities will grow. This will set an upper limit on the trapped flux that is feasible for this type of experiment.

Flux dissipation requires additional corrections to the radius inferred from the measured interior magnetic field. As we will see, if the apparent radius of the shell is increased by the skin depth, this flux is not dissipated but rather conserved over the increasing area. This turned out to be approximately another 10% effect for our experiment. We wanted to estimate the induced shell currents without resorting to a complicated 2-D computer model. We assumed a resistive wall and computed the  $\theta$  component of the skin current density necessary to cancel the measured axial magnetic field inside. To smooth out the necessary derivatives we first fitted a curve to the measured  $B_z(t)$  evolution (e.g. Fig. 5) from the magnetic coil probes. For axial flux compression, Ampère’s law  $\nabla \times \mathbf{B} = \mu_0 \mathbf{J}$  in cylindrical geometry is

$$dB_z/dr \approx B_z/\delta = \mu_0 J_\theta. \quad (8)$$

The induced current density  $J_\theta$  is assumed to exist in a layer one skin depth  $\delta$  thick on the inside surface of the cylinder. The skin depth  $\delta(t)$  was calculated from the zero order time dependent resistivity  $\eta(t)$  and scale time  $\tau(t)$ . One example is shown in Fig. 18 for the magnetic coil  $\dot{B}_2$  probe at a position  $z = -2.1$  cm from the midplane,

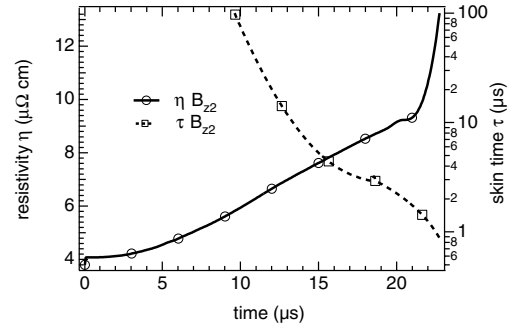


**Figure 18.** Time development of the calculated resistivity  $\eta(t)$  and scale time  $\tau(t)$  from curve fit data and heating of the shell from the SHIVA axial current. The temperature  $T(t)$  is proportional to  $\eta(t)$  and corresponds to a maximum of  $700^\circ\text{C}$  for this data set.

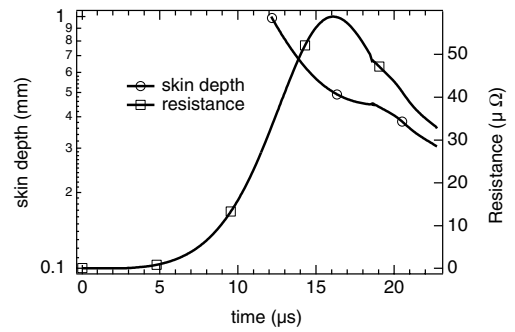


**Figure 19.** Typical time development of the calculated skin depth  $\delta(t)$  and resistance  $R(t)$  in the skin depth layer from curve fit data and heating of the shell from the SHIVA axial current.

$$\delta(t) \approx [2i\eta(t)\tau(t)/\mu]^{1/2}. \quad (9)$$

The timescale  $\tau \approx 1/\omega$  for changes in magnetic field has been computed as

$$\tau(t) = \frac{B_z^{(0)}(t)}{d[B_z^{(0)}(t)]/dt}. \quad (10)$$

The total azimuthal current in the skin layer must then be restricted to an area  $\delta(t)\Delta z$  (liner height) and was estimated as  $I_\theta(t) \approx J_\theta\delta(t)\Delta z$ . This image current  $I_\theta(t)$  increased to approximately 65 kA at the end of the shot. As functions of time, we numerically calculated from data and materials properties the dissipated power  $P_{diss}(t) = I_\theta^2(t)$ , loop resistance  $R(t) \approx \eta(t)2\pi r^{(0)}(t)/[\delta(t)\Delta z]$  and flux dissipation energy  $U_{diss}(t) = \int P_{diss}(t)dt$ . The computed skin depth  $\delta(t)$  is indicated on the left hand axis of Fig. 19, where the resistance  $R(t)$  is indicated on the right hand axis. It is interesting to note that, since the azimuthal path length around the circumference decreases at the end of the shot, the resistance decreases even though the resistivity increases for an ohmically heated conductor.

The radially compressing flux conserver does work on the interior magnetic field and compresses it to a smaller volume while adding extra energy

$$U_{PdV}(t) = \int [B(t)^2/2\mu_0]2\pi r dr dz.$$

For our time dependent data integrated inside the volume bounded by the flux conserver,  $U_{PdV} \approx 1.5$  J at the convergence

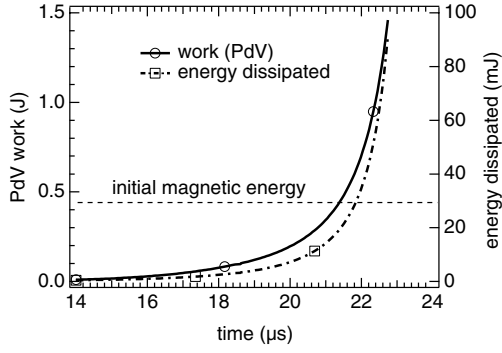


**Figure 20.** Typical time development of the calculated integrated  $P dV$  work on the flux conserver shell and the seed magnetic field inside it. On the right hand axis the dissipated ohmic heating of the liner accounts for the flux dissipation. For the much larger magnetic flux contained inside a compressed FRC, the flux expansion into the boundary would probably melt the shell at the end.

time as shown in Fig. 20. If we had been compressing an FRC with large magnetic field inside, the shell motion would have stagnated at the point where all the kinetic energy of the shell ( $\approx 1.4$  MJ in this case) was converted into magnetic energy. This limits the amount the internal flux can be compressed. To do a complete accounting of the energy one should include initial energy  $U_0$ , add magnetic pressure energy  $U_{PdV}(t)$  and then subtract the ohmically dissipated energy  $U_{diss}(t)$ , which is shown in Fig. 20. The seed magnetic field contains approximately  $U_0 \approx (20-30) \times 10^{-3}$  J. The total energy can be expressed as a magnetic energy where we invoke a total magnetic field  $B(t)$  that is trapped inside the moving flux conserver,

$$U(t) = U_0 + U_{PdV}(t) - U_{diss}(t) = \int [B^2(t)/2\mu_0] d^3x \\ = [B^2(t)/2\mu_0] \pi [r(t)]^2 \Delta z. \quad (11)$$

We will take our zero order assumption of no dissipation and later correct it for the magnetic field that actually diffuses into the resistive skin layer in the flux conserver. The ohmically dissipated energy  $U_{diss}(t)$  allows us to make a first order correction to our zero order assumption of no dissipation. Since we have already calculated the zero order radius assuming flux is conserved, the flux inside the flux conserver radius (to order zero) does not vary,

$$\Phi^{(0)}(t)/\Phi(t=0) \\ = B(t)[r^{(0)}(t)]^2/[B(t=0)r^2(t=0)] \approx 1 \quad (12)$$

and we can rewrite the energy equation (11) normalized to its initial value

$$U(t)/U_0 = B^2(t)[r^{(0)}(t)]^2/[B^2(t=0)r^2(t=0)].$$

This is approximately

$$U(t)/U_0 \approx B^{(1)}(t)/B(t=0)[\Phi^{(0)}(t)/\Phi_0] \\ \approx B^{(1)}(t)/B(t=0). \quad (13)$$

Therefore the corrected magnetic field that would exist if none of it diffused into the liner, i.e. if flux was conserved over the interior area of the liner, is to first order

$$B^{(1)}(t) \approx B(t=0)[U_0 + U_{PdV}(t) + U_{diss}(t)]/U_0 \quad (14)$$

and the first order radius is calculated using Eq. (7) but invoking  $B^{(1)}(t)$  this time,

$$r^{(1)}(t) \approx r(t=0)[B(t=0)/B^{(1)}(t)]^{1/2}. \quad (15)$$

Here we have added back in the missing ohmically dissipated energy (or the missing flux inside the flux conserver) that was not accounted for in  $B^{(0)}(t)$ . The  $B_z^{(1)}(t)$  data in Figs 5 and 13 and subsequent calculations have all been corrected with this factor so we can use Eq. (15), which is the analogue of Eq. (7) with the corrected magnetic field that we extract from the inferred energy dissipation. Our correction for  $B_z^{(1)}(t)$  is of the order of 10%, so that the radius  $r^{(1)}(t)$  consequently suffers a 5% correction. The complete numerical 2-D calculations [43, 46] would predict a 15% correction for  $B_z^{(1)}(t)$ .

Surprisingly, these corrections turn out to be equivalent to assuming that the axial flux is conserved, but over a larger area, i.e. inside a radius that is larger than the interior of the flux conserver by one skin depth. As a result of energy dissipation the flux spreads out — it does not actually disappear. One way to see this is to rewrite the magnetic energy equation (11) as  $U(t) = \Phi(t)[B(t)/2\mu_0]\Delta z$ . From this it is clear that with enough dissipation (i.e.  $U(t) \rightarrow 0$ ) the energy can vanish even though the flux  $\Phi(t)$  remains constant as long as  $B(t)$  vanishes. Equation (11) can also be rewritten  $U(t) = \Phi(t)^2(\Delta z/2\mu_0)/[\pi r(t)^2]$  so that the energy  $U(t)$  can also vanish for constant flux if it spreads out over a large enough area  $\pi r(t)^2$ .

## 4. Conclusion

The goal of these experiments was to demonstrate the feasibility of the first step on the route to MTF. We show here detailed data for a successful imploding flux conserving liner with the correct features to compress and heat through  $\int P dV$  the FRC target. What is new about these converging flux conserver liner experiments is the simultaneous achievement of the requisite long aspect ratio (3:1), radial convergence ratio ( $> 11:1$ ), circularity and uniformity ( $< 0.6\%$ ). In order to show that the one experiment was not a fluke, two successful liner shots (with no failures) were carried out, and both were quantitatively similar. Taccetti et al. [42] provide more detail for these experiments. Continuous time records of the trajectory of the liner are shown, and the snapshot data from X ray radiographs and FID fibre impact corroborate these data. The radial time history and velocity are consistent with a straightforward circuit model with no free parameters and the assumption of a non-compressible liner. We have outlined a straightforward series of calculations that estimate the internal fields, image currents and flux dissipation in the liner that do not require sophisticated computer modelling.

The next step for the liner programme would be to show that either continuously deformable electrical contacts at the ends of the liner, or a  $\theta$  pinch driven flux compressor can be successfully engineered. This would allow a larger entrance aperture to translate the FRC into the liner, and greatly simplify the electrical feed arrangement. Our seed magnetic field was 60–90 G, much smaller than the 5 T expected for our test FRC. The field compression factor of  $\approx 50-100$  would lead to 200–500 T in a compressed FRC. It is worth noting that

an explosively driven flux conserver with height to diameter ratio of 1.5:1 was imploded some 20 years ago, with a final compressed seed field inside of over 200 T [15].

Our next step at LANL for the MTF programme is to create a target FRC with sufficiently high density ( $n \approx 10^{17} \text{ cm}^{-3}$ ) and temperature ( $T_e \approx T_i \approx 250 \text{ eV}$ ) to translate into the liner interior. FRC experiments over 30 years ago [5, 21–25] showed high density target plasmas like this to be feasible. However, these plasmas were not well diagnosed for several reasons. Those experimenters did not realize that there was such a thing as a field reversed  $\theta$  pinch MHD equilibrium, and proceeded to their primary goal of generating neutrons. We hope to explore in detail the physics of high density FRCs.

### Acknowledgement

This work is supported by US Department of Energy (Office of Fusion Energy Sciences) Contract No. W-7405-ENG-36.

### References

- [1] Lindemuth I.R. et al 1995 *Phys. Rev. Lett.* **75** 1953
- [2] Siemon R.E., Lindemuth I.R. and Schoenberg K.F. 1999 *Comment. Plasma Phys. Control. Fusion* **18** 363
- [3] Ryutov D. and Siemon R. 2002 *Comment. Plasma Phys. Control. Fusion* in press
- [4] Gross R.A. 1975 *Nucl. Fusion* **15** 729
- [5] Kirkpatrick R.C. and Lindemuth I.R. 1991 *Fusion Technol.* **20** 834
- [6] Tuszewski M. 1988 *Nucl. Fusion* **28** 2033
- [7] Redfearn J. 1999 *Science* **286** 1829
- [8] Lindl J. 1995 *Phys. Plasmas* **2** 3933
- [9] Schoenberg K.F. and Siemon R.E. (eds) 1998 *Magnetized Target Fusion: A Proof of Principle Proposal, Report LA-UR-98-2413* Los Alamos Natl Lab., NM
- [10] Call C.J. and Moir R.W. 1990 *Nucl. Sci. Eng.* **104** 364
- [11] Siemon R.E. et al 1986 *Fusion Technol.* **9** 13
- [12] Tuszewski M. et al 1988 *Phys. Fluids* **31** 3754
- [13] Intrator T. et al 1999 *Bull. Am. Phys. Soc.* **44** 46
- [14] Faehl R. et al 1996 *Bull. Am. Phys. Soc.* **41** 1362
- [15] Armstrong W.T. and Morgan J.A. 1987 *Megagauss Magnetic Field Generation and Related Topics (Proc. 4th Int. Conf. Santa Fe, 1986)* (New York: Plenum) p 683
- [16] Barnes D.C. 1997 *Comment. Plasma Phys. Control. Fusion* **18** 72
- [17] Drake R.P., Hammer J.H., Hartman C.W., Perkins L.J. and Ryutov D.D. 1996 *Fusion Technol.* **30** 310
- [18] Eskov A.G. et al 1982 *Controlled Fusion and Plasma Physics (Proc. 10th Eur. Conf. Moscow, 1981)* vol 5G, part I (Geneva: European Physical Society) p 319
- [19] Wurden G.A. et al 2001 *Rev. Sci. Instrum.* **72** 552
- [20] Wurden G.A. et al 1999 *J. Plasma Fusion Res. SERIES* **2** 238
- [21] McLean E.A., Anderson A.D. and Griem H.R. 1967 *Pulsed High Density Plasmas (Proc. APS Top. Conf. Los Alamos, 1967)* LA-3770, Los Alamos Natl Lab., NM A5-1
- [22] Kolb A.C. et al 1966 *Plasma Physics and Controlled Nuclear Fusion Research 1965 (Proc. 2nd Conf. Culham, 1965)* (Vienna: IAEA) 261
- [23] Kaleck A. et al 1967 *Pulsed High Density Plasmas (Proc. APS Top. Conf. Los Alamos, 1967)* LA-3770, Los Alamos Scientific Lab., NM A4-1
- [24] Kaleck A. et al 1968 *Plasma Physics and Controlled Nuclear Fusion Research 1968 (Proc. 3rd Int. Conf. Novosibirsk, 1968)* vol 2 (Vienna: IAEA) p 581
- [25] Eberhagen A. and Grossman W. 1971 *Z. Phys.* **248** 130
- [26] Rej D.J. et al 1986 *Phys. Fluids* **29** 852
- [27] Rej D.J. et al 1992 *Phys. Fluids B* **4** 1909
- [28] Moses R.W., Krakowski R.A. and Miller R.L. 1979 *Conceptual Design of the Fast Liner Reactor (FLR) for Fusion Power, Report LA-7686-MS* Los Alamos Natl Lab., NM
- [29] Spencer R.L., Linford R.K. and Tuszewski M. 1983 *Phys. Fluids* **26** 1564
- [30] Parker J. 1993 *A Primer on Liner Implosions with Particular Application to the Pegasus II Capacitor Bank, ATHENA Technical Report No. 1* Los Alamos Natl Lab., NM
- [31] Reinovsky R.E. and Ekdahl C.A. 1996 *Megagauss Magnetic Fields and their Applications (Proc. 7th Int. Conf. Sarov, 1996)* VNIIEF, Sarov
- [32] Faehl R.J. et al 1997 *Pulsed Power (Proc. 11th IEEE Int. Conf. Baltimore, 1997)* (Piscataway, NJ: IEEE) 1375
- [33] Gerwin R.A. and Malone R.C. 1979 *Nucl. Fusion* **19** 155
- [34] Alikhanov S.G. et al 1983 *Plasma Physics and Controlled Nuclear Fusion Research 1983 (Proc. 9th Int. Conf. Baltimore, 1982)* vol 3 (Vienna: IAEA) 319
- [35] Degnan J.H. et al 1995 *Phys. Rev. Lett.* **74** 98
- [36] Degnan J.H. et al 1995 *Fusion Technol.* **27** 115
- [37] Degnan J.H. et al 2001 *IEEE Trans. Plasma Sci.* **PS-29** 93
- [38] Maisonnier C. et al 1966 *Rev. Sci. Instrum.* **37** 1380
- [39] Peterkin R.E., Frese M.H. and Sovinec C.R. 1998 *J. Comput. Phys.* **140** 148
- [40] Ruden E.L. and Bell D.E. 1997 *J. Appl. Phys.* **82** 163
- [41] Veaser L.R. et al 1987 *SPIE Proc. Conf.* **838** 60
- [42] Taccetti J.M. et al 2002 *Magnetic field measurements inside a converging flux conserver Fusion Eng. Des.* in press
- [43] Knoepfel H.E. 2000 *Magnetic Fields* (New York: Wiley)
- [44] Lochte-Holtgreven W. 1995 *Plasma Diagnostics* (New York: AIP) p 624
- [45] Weber, J.W. (ed) 1995 *CRC Handbook of Laser Science and Technology, Suppl. 2: Optical Materials* (Boca Raton, FL: CRC Press)
- [46] Somon J.P. 1968 *Sur l'Obtention de Champs Magnétique Intense au Moyen d'une Implosion Cylindrique, Rep. EUR 4197f* (Brussels: Euratom) (in French)